On Estimating Internal-Wave Energy Fluxes in the Ocean

JONATHAN D. NASH[1], MATTHEW H. ALFORD[2], AND ERIC KUNZE[3]

[1]*College of Oceanic and Atmospheric Sciences, Oregon State University, Corvallis.*

[2]*Applied Physics Laboratory and School of Oceanography, University of Washington, Seattle*

[3]*School of Earth and Ocean Science, University of Victoria, Canada*

(Manuscript received July 4, 2004, in final form March 13, 2005)

ABSTRACT

Energy flux is a fundamental quantity for understanding internal-wave generation, propagation and dissipation. In this paper, estimation of internal-wave energy fluxes $\langle \mathbf{u}'p' \rangle$ from ocean observations that may be sparse in either time or depth are considered. Sampling must be sufficient in depth to allow estimation of the internal-wave-induced pressure anomaly p' using the hydrostatic balance, and sufficient in time to allow phase averaging. Data limitations considered include profile time-series with coarse temporal or vertical sampling, profiles missing near-surface or near-bottom information, moorings with sparse vertical sampling, and horizontal surveys with no coherent resampling in time. Methodologies, interpretation and errors are described. For the specific case of the semidiurnal energy flux radiating from the Hawaiian Ridge, errors of ∼10% are typical for estimates from 6 full-depth profiles spanning 15 h.

1. Introduction

Energy flux $\mathbf{F_E} = \langle \mathbf{u}'p' \rangle = \mathbf{c_g}E$ is a fundamental quantity in internal-wave energetics to identify energy sources, wave propagation, and energy sinks. Internal-wave radiation transports energy from the boundaries into the stratified ocean interior for turbulence and mixing (Munk and Wunsch 1998). Arguably, it is the piece that is missing from 1-D boundary-layer parameterizations (e.g. Mellor and Yamada 1982; Price et al. 1986; Large et al. 1994; Baumert and Peters 2004; Johnson et al. 1994a,b), representing a potential sink of boundary energy in local budgets.

Until recently, internal-wave energy fluxes in ocean observations were estimated by measuring the energy and using the dispersion relation to quantify the group velocity (e.g. Kunze and Sanford 1984; Mied et al. 1986; Kunze et al. 1995; D'Asaro et al. 1995). This requires measuring the vertical, zonal and meridional wavenumbers – only possible in wave fields dominated by a single wave and sampled with profile surveys conducted rapidly enough to avoid temporal aliasing.

A more powerful and flexible means of estimating the net energy flux is with the velocity-pressure correlation $\langle \mathbf{u}'p' \rangle$. Here, the principal complications are estimating the internal-wave-induced baroclinic pressure perturbation p' and determining how to average over wave phase ϕ. For hydrostatic internal waves ($\omega \ll N$), the pressure anomaly p' can be obtained by vertically integrating full-depth profiles of density perturbation ρ' using the hydrostatic balance. There remains the problem of the integration constant (which can be thought of as the internal-wave-induced surface pressure perturbation).

Early work apparently didn't recognize the contribution from surface pressure so got the vertical distribution incorrect (Garcia Lafuente et al. 1999). However, Ray and Mitchum (1997) and Cummins and Oey (1997) recognized that the vertically-integrated baroclinic energy flux is independent of the integration constant since the depth integral of the baroclinic velocity vanishes $\int_{-H}^{0} \mathbf{u}'dz = 0$.

Kunze et al. (2002) took advantage of the fact that, like the baroclinic velocity, the baroclinic pressure perturbation also has zero depth average $\int_{-H}^{0} p'dz = 0$. This allows one to estimate the integration constant from full-depth profiles of density perturbations. They used their measurements to show that convergence of upcanyon energy flux in the deeper Monterey Submarine Canyon balanced turbulence dissipation rates. Carter and Gregg (2002) did the same in the shallow end of the canyon. Since then, similar energy-flux computations have been used to quantify internal tide generation at ridges in observations (Althaus et al. 2003; Rudnick et al. 2003; Lee et al. 2005; Nash et al. 2004a; Rainville and Pinkel 2005) and models (Merrifield et al. 2001; Merrifield and Holloway 2002; Simmons et al. 2004), to examine the loss

Corresponding author address: Jonathan D. Nash, 104 COAS Admin Bldg. Oregon State University, Corvallis OR, 97331
E-mail: nash@coas.oregonstate.edu

of a low-mode internal tide to high modes and turbulence over a near-critical continental slope (Nash et al. 2004b), to examine internal wave energy fluxes on a broad continental shelf (MacKinnon and Gregg 2003) and to quantify semidiurnal and inertial energy fluxes globally using historical mooring data (Alford 2003). Rigorous error estimates of $\mathbf{F_E}$ have not been made in the above studies.

In this paper, methodologies for calculating the internal-wave energy flux from ocean observations will be described (sections 2, 3). Uncertainties and biases introduced by limited temporal sampling in profile time-series are described in section 4 and those with sparse vertical sampling in current-meter moorings are described in section 5. Conclusions are presented in section 6. The effect of wave advection of horizontal density and velocity gradients is discussed in Appendix A. Our method of generating GM space/time-series is described in Appendix B.

2. The internal wave energy equation

The role of the energy flux $\mathbf{F_E} = \langle \mathbf{u}' p' \rangle = \mathbf{c_g} E$ can best be assessed from the internal-wave conservation of energy equation

$$\frac{\partial E}{\partial t} + (\mathbf{u} \cdot \nabla) E = \nabla \cdot \langle \mathbf{u}' p' \rangle + Q_+ - Q_- \qquad (1)$$

where $E = KE + APE$ is the energy density, $KE = \overline{\rho} \left(\langle u^2 \rangle + \langle v^2 \rangle + \langle w^2 \rangle \right) /2$ the kinetic energy density, $APE = \overline{\rho} \overline{N}^2 \langle \xi^2 \rangle /2 = \overline{\rho} \langle b'^2 \rangle / (2\overline{N}^2)$ the available potential energy density, $\partial E / \partial t$ the accumulation or depletion of energy density, Q_+ represents sources such as wind-forcing of near-inertial waves (D'Asaro et al. 1995; Alford 2003) or internal tide generation by tide/topography interactions (Bell 1975; Baines 1982; Ray and Mitchum 1997; Althaus et al. 2003), and Q_- sinks associated with loss to turbulent dissipation and the background geostrophic flow.

In a steady state balance, the energy flux represents transport of energy from sources Q_+ to sinks Q_-. In the context of the global internal-wave field, recent evidence indicates that sources can lie thousands of km away from sinks (Dushaw et al. 1995; Cummins et al. 2001; Nash et al. 2004b; Alford 2003), consistent with altimetric observations of the mode-1 internal tide radiating far northward from the Hawaiian Ridge (Ray and Mitchum 1997) and inferences of a near-inertial wave propagating $>$ 300 km from its source to its detection point (Alford and Gregg 2001).

a. Flux calculations

To compute the baroclinic energy flux, the internal-wave-induced perturbations in pressure p' and velocity $\mathbf{u}'$ must be inferred from density ρ and velocity $\mathbf{u}$ profiles. First, the density anomaly is estimated as

$$\rho'(z,t) = \rho(z,t) - \overline{\rho}(z), \qquad (2)$$

where $\rho(z,t)$ is the instantaneous measured density and $\overline{\rho}(z)$ is the time-mean vertical density profile. Alternatively, $\rho'(z,t)$ may be defined in terms of the vertical displacement of an isopycnal $\xi(z,t)$ relative to its time-mean position so that $\rho'(z,t) = (\overline{\rho}/g)\overline{N}^2 \xi(z,t)$.

The pressure anomaly $p'(z,t)$ is calculated from the density anomaly using the hydrostatic equation,

$$p'(z,t) = p_{surf}(t) + \int_z^0 \rho'(\hat{z},t)\, g\, d\hat{z}. \qquad (3)$$

Although the surface pressure $p_{surf}(t)$ is not measured, it can be inferred from the baroclinicity condition that the depth-averaged pressure perturbation must vanish:

$$\frac{1}{H} \int_{-H}^0 p'(z,t) dz = 0. \qquad (4)$$

The perturbation velocity is defined as

$$\mathbf{u}'(z,t) = \mathbf{u}(z,t) - \overline{\mathbf{u}}(z) - \overline{\mathbf{u}_o}(t) \qquad (5)$$

where $\mathbf{u}(z,t)$ is the instantaneous velocity, $\overline{\mathbf{u}}(z)$ is the time-mean of that velocity, and $\overline{\mathbf{u}_o}(t)$ is determined by requiring baroclinicity:

$$\frac{1}{H} \int_{-H}^0 \mathbf{u}'(z,t) dz = 0. \qquad (6)$$

The baroclinicity conditions (4) and (6) require full-depth profiles to determine the barotropic contribution. If data is obtained from a small number of discrete moored instruments, identifying the barotropic signal may thus be difficult.

Ocean variability spans a broad range of temporal and spatial scales. In the frequency domain, u and ξ are usually dominated by a few narrow peaks (often in tidal and inertial bands) overlying a broad red continuum (Fig. 1). If long and continuous time-series are available, the computation of $\mathbf{F_E}$ in any frequency band is straightforward. Unfortunately, data are usually sparse, so it is important to determine what sampling and averaging (i.e., $\langle ... \rangle$) is necessary for $\mathbf{F_E} = \langle \mathbf{u}' p' \rangle$ to represent a meaningful energy flux for the spectral peak of interest, and to place bounds on its accuracy. Moreover, a number of the quantities in (2), (3) and (5) are difficult to measure from sparse data. First, $\overline{\rho}(z)$, $\overline{p}(z)$, and $\overline{\mathbf{u}}(z)$ represent vertical profiles of an undisturbed water column in the absence of internal waves (i.e., $\overline{\mathbf{u}}(z) = T^{-1} \int_0^T \mathbf{u}(z,t) dt$ where T is the averaging interval, with $T \gg$ wave period). For coarsely sampled data, it may be difficult to differentiate the background state (which may be slowly varying due to mesoscale activity) from a wave-perturbed state.

The background state slowly evolves due to mesoscale processes. Typical geostrophic near-surface velocity and pressure fluctuations associated with a 50-km by 200-m deep feature are $u_{meso} \sim 0.2$m/s and $p_{meso} \sim 600$ Pa.

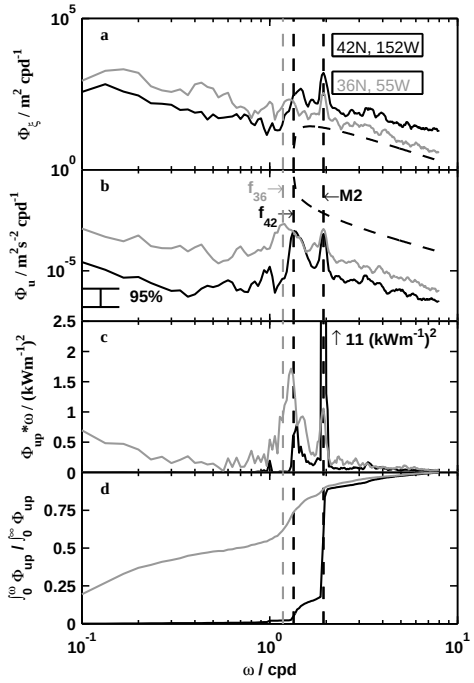

FIG. 1. Frequency spectra of mode-one amplitudes of (a) ξ and (b) u from sites in the North Pacific (6 instruments, 1984, black) and North Atlantic (4 instruments, 1976, gray) Oceans. Spectra were computed from the year-long time-series in overlapping 30-day blocks. Spectral peaks at semidiurnal and near-inertial frequencies dominate the variance of u and ξ. The latter tends to be weaker, broader and slightly superinertial, particularly for ξ. The energy flux is dominated by these two frequencies, as shown by the energy-flux spectrum (c), plotted in variance-preserving form ($\Phi_{up} \cdot \omega$). Note that the Pacific semidiurnal peak is $4\times$ full scale. Cumulative energy-flux spectra normalized by the total energy flux are shown in (d).

While these have the potential to produce instantaneous $\int u_{meso} p_{meso}\, dz \sim 1$ kW/m, the mesoscale contributions are at low frequency and spectrally distinct from the internal wave band (Fig. 1). Over short timescales, these act to define the mean, but do not alter internal-wave perturbation fields. Furthermore, u_{meso} scales with dp_{meso}/dy, not p_{meso}, so that extrema in p_{meso} occur at near-zero u_{meso} and vice versa. As a result, spatially integrating over a smooth geostrophic front produces $\iint u_{meso} p_{meso}\, dx\, dz = 0$. Mesoscale processes may also Doppler-shift narrowband peaks into broadband wavefields. In extreme cases, it may be most appropriate to use full spectral methods such as those of Rainville and Pinkel (2005) to compute energy fluxes.

In the following analysis, we treat the wavefield as a number of narrowband peaks superimposed onto a broadband continuum. To estimate $\mathbf{F_E}$ in a specific frequency band of interest, harmonic analysis or time-domain filtering must be performed to extract the frequency band of interest. Standard time-series techniques determine one's ability to separate different frequency constituents, as the frequency resolution is $\Delta\omega = 2\pi/T$, where T is the record length.

b. Example time-series

A synthetic time-space series of the internal wavefield based on a site of strong semidiurnal internal tide propagation is used to illustrate a number of aspects of the energy-flux calculation (Fig. 2). This wavefield is consistent with the density and cross-ridge velocity observations obtained at AVP station 14 (in Kauai Channel) on 28 October, 2000 during the Hawaii Ocean Mixing Experiment (Nash et al. 2004a; Lee et al. 2005). The station is located approximately 20 km from a major generation site of semidiurnal internal tides, and is characterized by strong depth-integrated energy flux (-19 kW/m), a vertical structure that exhibits both vertically-propagating and vertically-standing semidiurnal internal waves, and a weaker near-inertial signal that contains significant high-vertical-wavenumber shear, but little energy flux (< 1 kW/m). Both beams and low vertical modes contribute to the semidiurnal flux. Its characteristics are summarized in Table 1.

		M_2	near-f	GM
$2\,\frac{1}{2}\overline{\rho}\int N^2\langle\xi^2\rangle dz$	[kJ/m^2]	12.5	1.5	3.1
$\frac{1}{2}\overline{\rho}\int\langle u^2+v^2\rangle dz$	[kJ/m^2]	8.5	4.8	5.0
$\overline{\rho}\int\langle u'p'\rangle dz$	[kW/m]	-19.0	-0.36	0
$\overline{\rho}\int\langle v'p'\rangle dz$	[kW/m]	2.3	.68	0

Table 1. Energetics of each component of the synthetically generated time-space series, vertically-integrated over the $H = 3100$-m water depth. These correspond the benchmark case of $a_{M_2} = a_f = a_{GM} = a_{ins} = 1$; in the simulations to follow, the energy in each of these bands was varied from $0\times$ to $4\times$ these levels.

Fig. 2 displays the vertical and temporal structure of each wave component, and the interplay between these in forming the total energy flux. First we examine the vertical structure. The cross-ridge velocity u' and vertical displacement ξ (upper two rows) have similar vertical wavenumber content, but the amplitudes of u' scale with $\sqrt{N}$, while ξ scales with $1/\sqrt{N}$. Hence, u' is surface-intensified, while ξ is bottom-intensified. Since p' represents a vertical integral of ξ, its spectrum is redder by a factor of k_z^2 than that of isopycnal displacement ξ (or velocity u'). It is thus dominated by the lowest few modes. As a result, p' acts as a low-pass filter so that the $u'p'$ correlation is also dominated by low modes. Hence, only the low-mode component of u' contributes to $u'p'$ for typical u' and ξ (with spectra $\propto k_z^{-2}$).

A striking feature is that the total instantaneous energy flux $\langle u'p'\rangle$ (lower right panel; shading) is not equal to either the semidiurnal signal (lower left panel) nor the sum of semidiurnal, near-inertial and GM fluxes (lower right panel; solid line) despite the fact that the energy fluxes

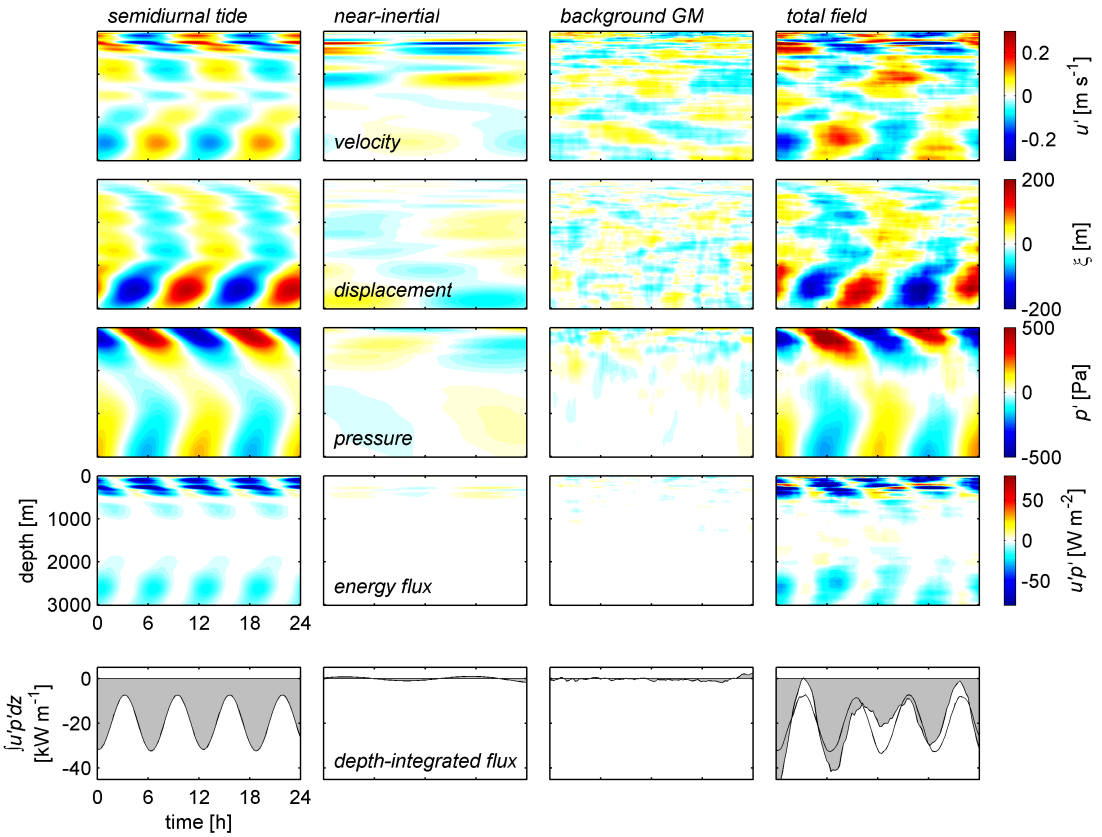

FIG. 2. Synthetically-generated time-space plots of velocity fluctuation (top row), vertical displacement (second row), pressure perturbation (third row) and energy flux (fourth row) consistent with observations at AVP station 14 during HOME 2000. The first two columns represent the semidiurnal (left) and near-inertial components (second from left) as determined by harmonic analysis to the u and ξ data. The third column represents a randomly-phased GM wavefield (see Appendix A for details). The rightmost column is the sum of semidiurnal, near-inertial and GM wavefields, so is a statistically consistent representation of the observed wavefield. Corresponding time-series of the depth-integrated energy flux are presented in the bottom row (shading); the solid line in the lower rightmost panel is the simple sum of the energy flux in the semidiurnal, near-inertial and GM wavefields. This is not equal to the energy flux of the combined wavefield (shading) because the instantaneous cross terms (i.e., $u'_{GM}p'_{M_2}$) do not vanish. Note that the instantaneous $\mathbf{u}'p'$ varies as $\cos^2(\omega t + \phi)$, so that appropriate averaging is necessary to produce meaningful estimates of $\mathbf{F_E}$.

in the near-inertial and GM fields are very weak. This is because the total instantaneous energy flux is not a linear combination of the constituent fluxes but a quadratic quantity containing cross-terms, as illustrated below.

The observed oceanic velocity and pressure perturbation may be written as

$$u' = u'_{M_2} + u'_f + u'_{GM} + u'_{adv} \tag{7}$$

$$p' = p'_{M_2} + p'_f + p'_{GM} + p'_{adv} \tag{8}$$

where M_2, f and GM represent the semidiurnal, near-inertial and Garrett-Munk variability; adv represents the contribution to u' and p' from the horizontal advection of low-frequency features by wave motions (see Appendix A). The total energy flux is then:

$$\begin{aligned} u'p' = {} & u'_{M_2}p'_{M_2} + u'_f p'_{M_2} + u'_{GM}p'_{M_2} + u'_{adv}p'_{M_2} \\ & + u'_{M_2}p'_f + u'_f p'_f + u'_{GM}p'_f + u'_{adv}p'_f \\ & + u'_{M_2}p'_{GM} + u'_f p'_{GM} + u'_{GM}p'_{GM} + u'_{adv}p'_{GM} \\ & + u'_{M_2}p'_{adv} + u'_f p'_{adv} + u'_{GM}p'_{adv} + u'_{adv}p'_{adv} \end{aligned} \tag{9}$$

While $u'_{M_2}p'_{M_2}$ is the leading term, the instantaneous off-diagonal contributions are not negligible, as illustrated by comparing the right and left columns of Fig. 2. For a long, well-sampled time-series, these contributions average to zero, so that perfect sampling produces unbiased results. It is the purpose of the following sections to determine the error and bias for the case where sampling is sparse in either the spatial or temporal domains.

Although the following analysis focuses on the semidiurnal waveband (as it is often the most energetic – Fig. 1), these techniques apply equally well to spectral peaks at other frequencies. And while the chosen vertical structure and phasing of u' and ξ is consistent with a site dominated by M_2 variance, we assess the error for a wide range of relative amplitudes of semidiurnal, near-inertial and GM signals, making this analysis applicable to sites where semidiurnal velocity variability is not dominant.

3. Calculations

If all terms in (2)–(6) are fully-resolved, the x-component of the vector energy flux may be calculated as a simple average of fluctuating covariance:

$$F_E(z) = \langle u'(z)p'(z)\rangle. \tag{10}$$

For a narrowband wavefield, perhaps dominated by near-inertial or semidiurnal waves as is often the case in the ocean, averaging $\langle ...\rangle$ is optimal over an integral number of wave periods. For a single propagating wave, $u' = u'_o\cos(kx+mz-\omega t-\phi_u)$, phase-averaging can be accomplished by averaging in the horizontal x, depth z or time t. For a vertically-standing wave, $u' = u'_o\cos(kx - \omega t - \phi_u)\cos(mz)$, phase-averaging must be over distance x (or time t) and depth z. For a horizontally-standing wave, $u' = u'_o\cos(mz - \omega t - \phi_u)\cos(kx)$, phase-averaging must be over depth z (or time t) and distance x. For a broadband wavefield with no single spectral peak, time-series measurements of sufficient resolution and duration to cover all frequencies are needed and the energy flux is best determined spectrally.

Since oceanic measurements cannot span an integral number of periods for all waves of interest, the sample mean $\overline{u(z)}$ will contain a contribution from the wavefield itself. If the wavefield is dominated by a few spectral peaks (Fig. 1), harmonic analysis can efficiently extract the mean and perturbation quantities from relatively coarse-resolution observations, i.e.,

$$u(z,t) = \overline{u}(z)+u'_o(z)\sin(\omega t-\phi_u(z))+R_u(z,t) \tag{11}$$

where the amplitude $u'_o(z)$ and phase ϕ_u and $\overline{u}(z)$ are determined through a least-squares minimization of the residual $R_u(z,t)$. By performing a similar harmonic analysis to $p'(z,t)$, a narrowband estimate of the semidiurnal energy flux may be computed as

$$F_E^{M_2}(z) = u'_o(z)p'_o(z)\cos(\phi_u(z) - \phi_p(z)) \tag{12}$$

where p'_o and ϕ_p represent the semidiurnal amplitudes and phases of the pressure perturbation.

4. Data with coarse temporal sampling

In this section, we illustrate how coarse temporal sampling affects the error in $\langle u'p'\rangle$ estimates. A framework is presented to quantify the standard error given a dataset completely resolved in depth but coarsely resolved in time such as that obtained from freefall profilers (e.g., AVP, XCP, HRP) or shipboard LADCP/CTD. We then apply this framework to a synthetically-generated profile time-series to illustrate the effects of temporal sampling for several different baroclinic tide regimes.

We wish to compute the time-average energy flux in a single frequency band. In the following, we consider the semidiurnal waveband, denoted as $\langle u'_{M_2}p'_{M_2}\rangle$, although the analysis pertains equally well to any frequency waveband. If the wavefield is dominated by semidiurnal variance, then harmonic analysis to as few as four profiles over a 12.4-h period may extract the signal if phasing of the sampling is fortuitous. Error will be decreased by increasing the number of samples and/or time-series duration. It is the purpose of this section to establish error bounds on such a calculation, and to help guide sampling strategies.

Without rapidly-acquired time-series or *a priori* knowledge of the frequency content, it is not possible to determine how much signal has been aliased into the data from non-semidiurnal constituents. One means of estimating the contamination is through statistics from data-inspired Monte-Carlo simulations. We apply the following procedure to our observational datasets:

1. at each depth, perform a harmonic analysis using as many frequency constituents as the data allows (i.e., $(n-1)/2$ frequencies or less, where n is the number of samples). Resolved time-series or physical intuition should guide the choice of frequencies. Equivalently, harmonic analysis may be performed on time-series of vertical mode amplitudes. In the following, we consider the semidiurnal and near-inertial bands, shown in mooring records to dominate the variability near the Hawaiian Ridge (i.e., Levine and Boyd 2004).

2. for the purpose of error analysis, assume that the above harmonic analyses have captured all of the narrowband variance. Many realizations of synthetic time-series may then be generated by adding random barotropic phases to each frequency component; a randomly-phased broadband GM wavefield is also added (see Appendix B).

3. compute error statistics by sampling time-space realizations consistent with the observations.

In the following, we use data from the Hawaii Ocean Mixing Experiment to illustrate the above procedure and to determine the error associated with typical energy-flux calculations. time-series of full-depth density and velocity were acquired with the Absolute Velocity Profiler (AVP; Sanford et al. 1978, 1985; Lee et al. 2005) at the 3000-m isobath in Kauai Channel during October 2000. This site (Station 14; Nash et al. 2004a; Lee et al. 2005) represents one of strong internal tides (-19 kW/m depth-integrated) and significant near-inertial activity.

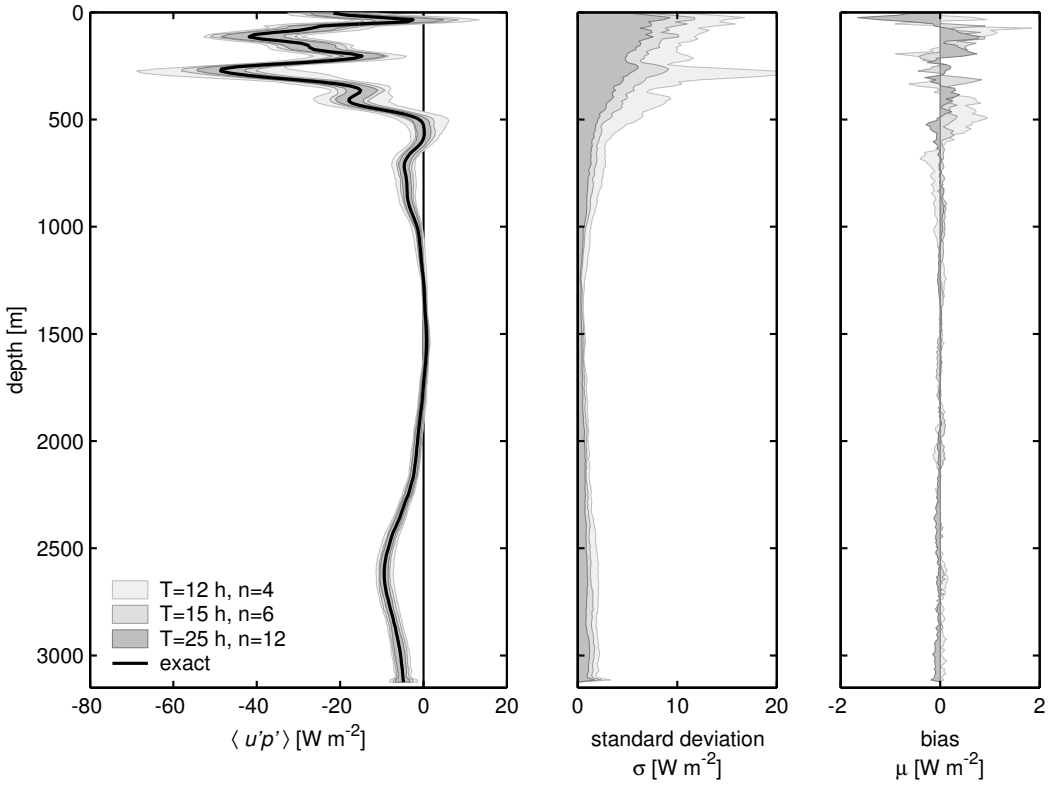

FIG. 3. Vertical energy-flux profile (left), standard error estimates (center) and bias (right) as computed from 200 realizations of a synthetically-generated space/time-series. Time-Series have random phase of all components, but are statistically consistent with the off-ridge component of the energy flux at AVP station 14, HOME 2000. The shading corresponds to three types of sampling, minimal (4 samples over 12 hours), efficient (6 samples over 15 h) and well-sampled (12 samples over 25 h). The solid line represents the prescribed semidiurnal energy flux.

At HOME AVP station 14, six full-depth profiles over a ∼15 hour period were acquired. Data were processed as outlined in the previous section and $\mathbf{u}'$ and ξ were computed for each profile. Harmonic analyses were performed to determine the amplitude and phase at semidiurnal and inertial frequencies so that the measured velocity is $u' = u'_{M_2} + u'_f + R_u$ and vertical displacements $\xi' = \xi'_{M_2} + \xi'_f + R_\xi$, where R_u and R_ξ represent least-squares minimized residuals. For simplicity, we consider only the cross-ridge component of velocity and energy flux in the following analysis, with $\hat{x}$ defined as 37° E of N; this is roughly aligned with the depth-averaged semidiurnal energy flux at this site.

We employed Monte-Carlo methods to test the sensitivity of the energy-flux calculation to various sources of contamination. Synthetic time-series were generated with different strengths of each semidiurnal, GM, near-inertial and instrument noise components. Time-Series of velocity and vertical displacement were generated as

$$u'_{test} = a_{M_2} u'_{M_2} + a_f u'_f + a_{GM} u'_{GM} + u'_{ins} \qquad (13)$$

and

$$\xi'_{test} = a_{M_2} \xi'_{M_2} + a_f \xi'_f + a_{GM} \xi'_{GM} + \xi'_{ins} \qquad (14)$$

where the a_n are nondimensional amplitudes that represent the strengths of the internal wavefield components relative to the values in Table 1. Each a_n represents a wave amplitude, so that the energy or energy flux associated with each contribution scales with a_n^2 and not with a_n (i.e, $\mathbf{F_E} \propto a_{M_2}^2$). A random instrument noise of $u'_{ins} = 0.02$ m/s and $\xi_{ins} = 0.5$ m was arbitrarily prescribed and added to the wavefields with insignificant effect on the flux estimates.

First, benchmark synthetic time-series of u_{test} and ξ_{test} were generated using $a_{M_2} = a_f = a_{GM} = a_{ins} = 1$, and estimates of $\langle u'p' \rangle$ computed using three sampling strategies: minimal (4 profiles in 12 hours), efficient (6 profiles over 15 hours), and well-sampled (12 profiles over 25 hours). In each case, 200 energy-flux estimates were computed from harmonic analyses that extract the semidiurnal signal (12); the near-inertial signal was also extracted for $n > 5$. Vertical profiles of the energy flux, standard error and bias, computed through M_2 harmonic

analyses for these three cases are shown in Fig. 3. A number of observations are immediately evident. The first is that even the minimal strategy qualitatively captures the vertical structure of the energy flux. Second, the standard deviation scales with the magnitude of the energy flux – that is, the error is smallest at mid-depths where the energy fluxes are the weakest, with 20% error being typical for a single depth estimate. Next, the sampling does not systematically bias the estimates; any bias is a factor of 10 less than the scatter. Finally, while increasing the number of samples and duration does reduce error, the gain in increasing the sampling from 6 in 15 h to 12 in 25 h is only marginal. This highlights the effectiveness of harmonic analysis to extract the desired signal (semidiurnal in this case).

To determine the sources of contamination, a sensitivity study was performed in which the strengths of the semidiurnal, GM, and near-inertial components were independently varied while holding the strength of each remaining internal wavefield constant. That is: (1) a_{M_2} was varied from 0 to 2 while $a_f = a_{GM} = 1$; (2) a_{GM} was varied from 0 to 2 while $a_f = a_{M_2} = 1$; and (3) a_f was varied from 0 to 2 while $a_{M_2} = a_{GM} = 1$. For each combination of a_{M_2}, a_f and a_{GM}, 200 realizations of u'_{test} and ξ_{test} were generated with (13) and (14) using random phasings of each wave component. These were then sampled according to each of our sampling strategies outlined in the following subsections, and statistics of the depth-integrated energy flux $\int F_E dz$ computed to diagnose the sources and magnitude of error and bias. Estimates were computed using both simple averages (10) and from harmonic analyses (12).

The cross-ridge energy flux was computed from either the simple average of the perturbation quantities as F_E (10) or from an harmonic analysis as $F_E^{M_2}$ (12). The standard deviation σ and bias μ of $\int F_E dz$ or $\int F_E^{M_2} dz$ was then computed from 200 independent realizations of the wavefield, and divided by the prescribed $\int F_E^{M_2} dz$ to yield the fractional error and bias. Using this definition, energy fluxes are considered biased if near-inertial signal aliases into our estimates. Results are shown in Figs. 4 – 6 and Tables 2 – 4. Lines in each figure represent the sensitivity of the fractional error or bias to the amplitude of semidiurnal signal (a,b) or contamination [GM (c,d) or near-inertial (e,f)] for a particular sampling strategy.

In the following, we investigate errors and bias associated with two types of oceanic observations. The first is sampling over a short duration (12–24 h) using a uniform $\sim$ 3-h time-step (section 4a). This is common of intensive process studies (i.e. Kunze et al. 2002; Althaus et al. 2003; Nash et al. 2004b,a) designed to capture a snapshot of the spatial structure of an internal wavefield. The second is data collected at irregular sampling intervals (section 4b). This represents data-of-opportunity, such as that obtained during WOCE transects where sampling is irregular in time or space with few repeated stations.

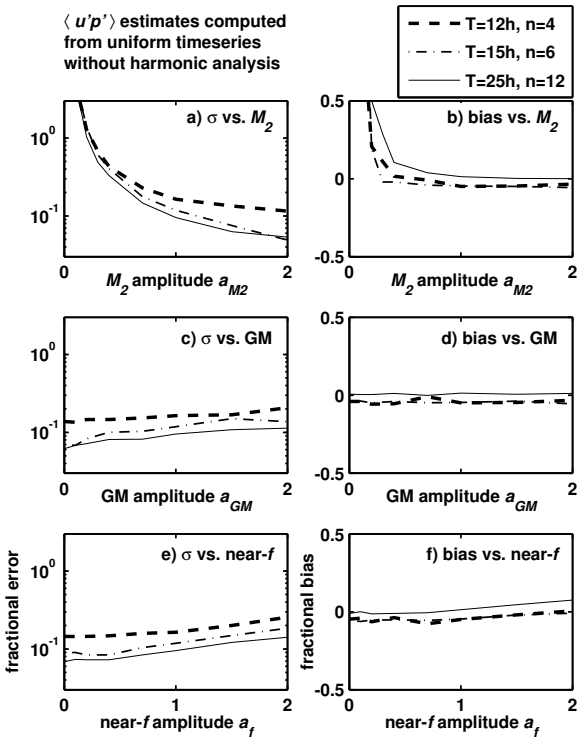

FIG. 4. Sensitivity of error and bias of the depth-integrated energy flux to the strength of (a,b) the semidiurnal, (c,d) GM, and (e,f) near-inertial components. Each data point represents the fractional standard deviation or bias as estimated from 200 realizations of a synthetically-generated space/time series with specific amplitudes of semidiurnal, GM and near-inertial signals (see text for details). For each realization, the synthetic data was sampled n times at equal intervals during the period T, and the energy flux calculated as the vertical integral of $F_E(z) = \langle u'(z)p'(z) \rangle$ (10), where $\langle \cdot \rangle$ represents a simple average of the n energy-flux estimates. Data is statistically consistent with AVP station 14, HOME 2000.

a. Regularly sampled time-series

We first consider the case of a time-series sampled n times at equal intervals over the period T. Synthetic time-series were sampled using one of the three sampling strategies (minimal, efficient or well-sampled), from which statistics of the energy flux were calculated as simple averages (Eq. (10), Fig. 4 and Table 2) or from harmonic fits (Eq. (12), Fig. 5 and Table 3).

For the benchmark case of $a_{M_2} = 1$, the error in $\int \mathbf{F_E} dz$ is $9 - 16\%$ and bias is less than 5%, with lower percentages corresponding to increased n. Using simple averages, the GM and near-inertial wavefields contribute to the error with similar magnitude. Harmonic analysis is able to reject near-inertial contamination almost completely for $n \geq 6$, since such sampling permits both M_2 and near-inertial harmonic analyses to be performed at this latitude. In contrast, a harmonic analysis cannot ex-

wave strength			fractional error (%)			fractional bias (%)		
a_{M_2}	a_{GM}	a_f	$T = 12$h $n = 4$	$T = 15$h $n = 6$	$T = 24$h $n = 12$	$T = 12$h $n = 4$	$T = 15$h $n = 6$	$T = 24$h $n = 12$
1	1	1	16	12	9.5	-4.9	-4.6	1.3
0.4	1	1	43	40	33	1.6	-2	10
1	0	1	14	7	6.2	-4	-4.4	0.73
1	1	0	14	8.9	6.9	-4.7	-5.3	-1.1

Table 2. Fractional error and bias for energy fluxes computed without harmonic analyses expressed as percentages; regular sampling intervals.

wave strength			fractional error (%)			fractional bias (%)		
a_{M_2}	a_{GM}	a_f	$T = 12$h $n = 4$	$T = 15$h $n = 6$	$T = 24$h $n = 12$	$T = 12$h $n = 4$	$T = 15$h $n = 6$	$T = 24$h $n = 12$
1	1	1	15	8.9	6.1	-0.31	-0.23	-0.058
0.4	1	1	40	25	14	2.1	0.17	0.035
1	0	1	10	0.88	0.48	-0.21	0.061	0.0026
1	1	0	11	9.1	5.7	0.7	0.26	-0.47

Table 3. Fractional error and bias for energy fluxes computed using M_2 harmonic analyses expressed as percentages; regular sampling intervals.

wave strength			fractional error (%)			fractional bias (%)		
a_{M_2}	a_{GM}	a_f	$n = 4$	$n = 8$	$n = 24$	$n = 4$	$n = 8$	$n = 24$
1	1	1	34	22	12	-22	-12	-3.6
0.4	1	1	58	42	26	-11	-7.1	8.2
1	0	1	36	22	12	-24	-9.5	-2.1
1	1	0	30	20	10	-29	-11	-2.5

Table 4. Fractional error and bias for energy fluxes computed without harmonic analyses expressed as percentages; random temporal sampling.

tract near-inertial variance for $n = 4$, nor can it reject GM contamination which is broadband and aliases into the M_2 band from many frequencies. The GM wavefield hence contributes most to the error.

Bias is substantially reduced through harmonic analysis for two reasons. The first is because energy-flux estimates from simple averages contain contributions from all frequencies, including near inertial. In the example presented here, the near-inertial contribution has the same sign as the M_2 energy flux, and hence the estimates are biased high. The near-inertial energy flux is 1.9% of the M_2 for the benchmark case (Table 1); whereas our bias estimates for the well-resolved $n = 12$ case is 1.3%.

Bias also results from error in the sample mean $\overline{u}$ and $\overline{p}$, which is subtracted from the observations to determine perturbations. Any such error reduces the variance of the perturbations.[1] This produces a bias towards lower energy fluxes, which we find for all poorly-sampled estimates ($n < 12$). Only for the case of $a_{M_2} = 0.4$ are the energy fluxes biased consistently high. This bias results from the near-inertial contribution, which carries 12% of the energy flux for $a_{M_2} = 0.4$ (ie., $\langle u'_{M_2} p'_{M_2} \rangle = -3$ kW/m, whereas $\langle u'_f p'_f \rangle = -0.36$ kW/m). These trends are evident in Fig. 4b and reduced through harmonic analysis (Fig. 5b).

We conclude that harmonic analyses are effective in extracting the M_2 signal from one contaminated with GM and near-inertial waves. For large energy fluxes, such as those in HOME, a harmonic analysis to as few as $n = 4$ samples provides a reliable estimate of $\int F_E dz$. For weaker fluxes (i.e., $a_{M_2} = 0.4$, $\int F_E dz = 3$ kW/m), $n \geq 6$ is required to reduce the error to 25% or less. We emphasize that these error bounds are based on depth integrals over a 3100-m water column, with GM and near-inertial wavefields specific to the Hawaiian Ridge. We also note that harmonic analyses can only be performed on profiles collected at the same location, since temporal phase is distorted if profile locations are displaced an appreciable fraction (i.e., >10%, ~ 15 km) of the dominant horizontal wavelength.

Aspects of this analysis may be specific to the HOME site. First, the separation of near-inertial and semidiurnal frequencies depends on latitude. Second, the spectral bandwidth of these peaks changes with location (i.e., distance from generation site, mesoscale intensity, degree of Doppler-shifting, etc.). Both factors alter the effec-

[1] The unbiased estimator of the variance of a random variable is $(n-1)^{-1} \sum_{i=1}^{n} (x_i - \overline{x})^2$ (i.e. Emery and Thomson 2001, pg. 229) so that there is a $1/n$ reduction in the covariance if simple averaging is used to estimate $\langle u'p' \rangle$ from n samples.

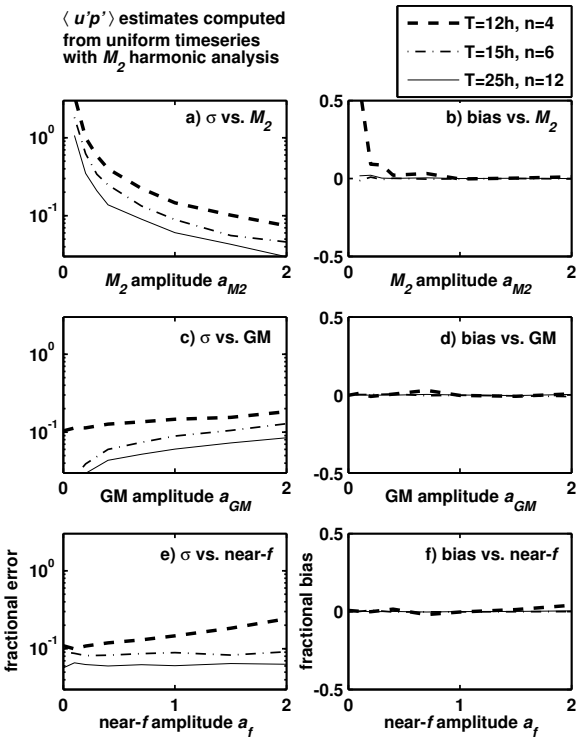

FIG. 5. As in Fig. 4 except that each energy flux estimate is based on an M_2 harmonic analysis of $u'(z)$ and $p'(z)$ to n equally-spaced samples over the period T. The energy flux is then the vertical integral of $F_E^{M_2}(z) = u_o(z)p_o(z)\cos(\phi_u(z) - \phi_p(z))$ (12).

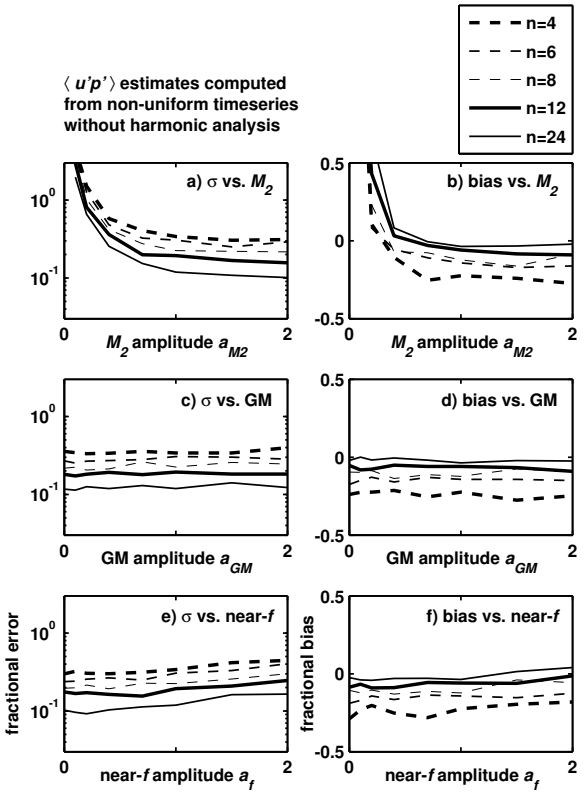

FIG. 6. As in Fig. 4 except that each energy flux estimate is based on the simple average (10) of n samples of the wavefield at random times during a 30-day period.

tiveness of harmonic analyses to extract a signal of interest. At high latitudes, for example, it may be impossible to distinguish semidiurnal from near-inertial variability if the time-series duration $T < 2\pi/(\omega_{M_2} - f)$.

b. Incoherently sampled wave field

We now consider the case of a space- or time-series sampled n times at irregular intervals over some long spatial or temporal period. While not an ideal sampling scheme, this section is included because data of this type is being re-analyzed to extract internal wave fluxes. For example, spatial transects with periodic CTD/LADCP data may be considered as a random collection of independent profiles. Such sampling does not capture all phase of the M_2 signal equally, and alters the sample estimates of both the mean and perturbation fields. Here, we consider n=4, 6, 8, 12, or 24 profiles acquired at random times over a $T = 30$-day duration (with a minimum $\Delta T = 3$ h between profiles). These may represent profiles acquired at a single location over a long duration, or at a number of different locations over which the internal wavefield may be considered homogeneous. The length of the total sampling period is unimportant, provided each wavefield is stationary and randomly phased (as we assume). Statistics of the energy flux are shown in Fig. 6 and Table 4 for simple average estimates.

A comparison of Fig. 6 (Table 4) with Fig. 4 (Table 2) indicates the error and bias for n profiles acquired randomly are 2-3 times larger than those obtained at regular intervals. Also note that these estimates assume stationarity of the wavefield over the sampling period. Given the intermittency of the internal tide (Wunsch 1975) on O(5 day) timescales, T should be chosen as short as possible while still permitting an appropriate n.

5. Data with imperfect vertical sampling

Vertical deficiencies of typical ocean data fall into two general categories: sparse, discrete measurements at a number of depths (e.g. moorings), and highly-resolved data over a portion of the water column (e.g. profiles). We will consider these two cases separately, assuming that the data are perfectly well-sampled in time. (For discrete-depth moorings, this is generally an excellent assumption.) In this case, contamination by motions of other frequencies (e.g. GM background and near-inertial signals) is less of an issue, since these signals can be removed by filtering or harmonic analysis. Otherwise, the

principles in the previous section apply.

As discussed earlier, the determination of baroclinic pressure anomaly requires full-depth, continuous data. Since neither type of moored dataset satisfies this requirement, we rely on normal modes to generate the full-depth profiles. Success will depend on the density of the sampling and the redness of the ocean vertical wavenumber spectrum at the frequency of interest.

The modal amplitudes are determined at each measurement time by solving a weighted least-squares problem,

$$u(z_i,t) = \sum_{j=0}^{M} \hat{u}_j(t) Z_j^u(z_i) \tag{15}$$

$$\xi(z_i,t) = \sum_{j=1}^{M} \hat{\xi}_j(t) Z_j^\xi(z_i), \tag{16}$$

where $\hat{u}_j$ and $\hat{\xi}_j$ are the j^{th} modal amplitudes of velocity and displacement at each time, and $Z_j^u(z)$, $Z_j^\xi(z)$ are the normal-mode structure functions. For velocity, the zeroth mode is rigorously the barotropic mode. Each set of i equations (one for each measurement depth) can be put in matrix form, and solved using standard overdetermined inverse methods (Dushaw et al. 1995). Formally, M_{meas} instruments can resolve M_{meas} modes. In practice, the specific mooring geometry and the shape of the spectrum can further limit this value.

In analogy with the temporal case, contamination arises when unresolved variance is projected onto resolved modes. The severity of the problem depends on the redness of the ocean spectrum, the geometry of the vertical sampling, and, in some cases, the number of modes being solved for. The aim of this section is to provide guidance in both designing vertical arrays and interpreting flux measurements of opportunity with imperfect sampling. Therefore, in parallel with the previous section, we conduct Monte-Carlo simulations of energy-flux calculations. For each combination of spectral redness and mooring geometry, a synthetic signal was generated by superposing thirty modes with random phases for velocity:

$$u(z,t) = \sum_{j=0}^{30} u_o j^q Z_j^u(z) \cos(M_2 t - \phi_j^u), \tag{17}$$

and displacement:

$$\xi(z,t) = \sum_{j=0}^{30} \xi_o j^q Z_j^\xi(z) \cos(M_2 t - \phi_j^\xi) \tag{18}$$

The parameter q governs the partition of energy among the modes. It is not known *a priori* , but will vary from place to place and in time. Guided by HOME data, we choose values of q spanning -1, the observed HOME value.

Several schemes for randomizing phase were employed, none of which materially affected our results. Completely randomizing the phase of all the modes would cause the "true" flux in each realization to vary wildly. To avoid this, we chose to fix the phase of the second mode relative to the first, so that the integrated flux in each realization was near -19 kW/m, as in the previous section.

For each pairing of vertical geometry and spectral redness, 100 realizations of synthetic data were generated, and the flux was computed over one M_2 cycle for each using the discrete and a perfectly-resolved array. The fractional bias and standard error were computed for each as the mean and standard deviation of the flux difference between the discretely-sampled and perfect arrays.

a. Sparse vertical sampling

We first consider fluxes determined from current and density measurements at discrete depths. To collapse the infinite number of possible mooring geometries into a spannable parameter space, we assume that the instruments are "ideally situated," which we define to be evenly spaced in a WKB-stretched depth coordinate z', defined as

$$z' = \int_0^z \frac{N(z^*)}{\overline{N}} dz^*.$$

In this coordinate, the modes are nearly sinusoidal and the instruments, at $z'_{ins} = (H/M_{meas})[(1,2,3,...M_{meas}) - 1/2]$, are located to best resolve them. Since it is generally desirable to resolve the dynamical modes, most moorings are designed with this in mind.

The fractional error and bias resulting from various numbers of ideally-spaced instruments are shown in figure 7. For each number of instruments M_{meas}, M_{meas}-2 modes were solved for (as will be seen in the next section, solving for fewer modes results in a moderate decrease in precision but can result in greater stability). Each curve represents a different spectral redness, where the HOME case is in the middle. With 40 instruments, error and bias are zero for all input spectra since more modes are resolved than are present in the ocean spectrum (30). As the number decreases, bias remains near zero, but the standard error increases, reaching 0.75 for four instruments in a spectral slope of -1. Thus, the number of realizations required for stable averages grows for sparse moorings. The lack of bias indicates that long-term averages will eventually converge on the correct value.

These errors and biases are for an estimate of the flux in a single M_2 cycle. Since the fractional errors for small instrument number approach unity, it desirable to know how much averaging is required to yield more precise estimates. Obviously, the error decreases as the square root of the number of independent observations. Unfortunately, the decorrelation timescale of the high-wavenumber contaminants is unknown. For example, if

a phase-locked internal-tide beam lying outside or on the edge of the instruments' range is the source of the contamination, no amount of averaging will help. At the opposite extreme, if the phase of the high-wavenumber motions is random from one cycle to the next, then the error in each single-cycle flux estimate will be uncorrelated. In this case, the fractional error in an average over, say 4 days, will be ≈ 3 times lower than the values cited here. In practice, this is likely to be about as good as can be done, since flux itself is variable on these time scales (Wunsch 1975; Alford 2003).

b. Profiles with gaps at the top or bottom

Since energy flux WKB-scales as buoyancy frequency N, it is typically extremely surface-intensified. Consequently, the calculation can become unstable without measurements close to the surface. Here we consider the effects of a gap at the top of an otherwise well-resolved profile. The stability of the calculation depends in this case on the number of modes to be solved for. Therefore, we present results for 2-, 4- and 8-mode solutions (Figure 8). Considering the former first (top panels), errors grow as the top instrument is deepened, but again bias remains nearly zero except for the "bluest" case. By 250 m, the fractional error is unity for the HOME case.

Increasing the number of modes to be solved for (middle, lower panels) decreases the error for small top gaps, as it does for well-instrumented discrete arrays (not shown). This is because the higher modes are better resolved and cannot project onto the flux-carrying low modes, introducing errors. However, solving for more modes carries the penalty of decreasing stability, as evident in the much larger errors and strong biases in the 8-mode case, when solving for more modes. That is, higher-mode solutions are more precise but more sensitive to gaps.

Much larger gaps at the bottom are tolerable (Figure 9). This is to be anticipated, given that the upper water column is weighted more strongly in WKB-stretched coordinates. The results are generally similar to the top-gap case, but much larger distances from the bottom are spanned. In the 2-mode case, fractional error is nearly constant at 0.3-0.4 even when only 4300 - 3000 = 1300 m of the water column is spanned. This is due to the surface intensification of the flux profiles and the dominance of the lowest modes in carrying the flux. Higher-mode solutions, as before, yield greater precision for full-column coverage but earlier instability and greater errors as the gap is increased.

6. Discussion

A framework for assessing the error and bias of baroclinic energy-flux estimates has been presented. Our method employs data-based Monte-Carlo simulations to assess the magnitude and parameter dependence of flux estimates made from a) temporally or b) vertically imperfect data.

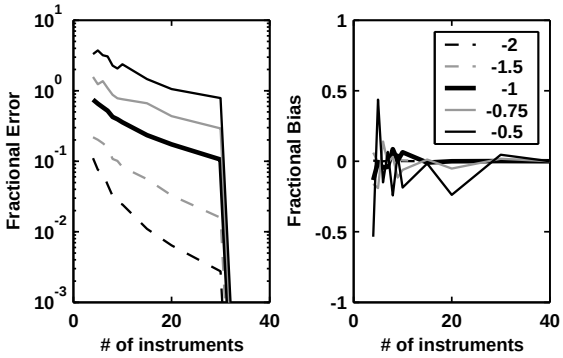

FIG. 7. Fractional error (left) and bias (right) of energy flux determined from Monte-Carlo calculations from a vertically-sparse mooring with perfect temporal resolution. Calculations are performed for a varying number of discrete vertical measurements (x axis). The different curves correspond to different spectral slope (p; legend) of the simulated signals. The redder the spectrum, the fewer instruments are required.

In the former case, we conducted simulations by varying M_2, GM and near-inertial energy about realistic values. We find that a 10% error is typical for estimates based on $n = 6$ profiles spanning 15 h, such as those collected with AVP during the Hawaii Ocean Mixing Experiment (Rudnick et al. 2003; Nash et al. 2004a; Lee et al. 2005)

In addition, we conclude that:

- unbiased semidiurnal energy-flux estimates can be computed from $n = 4$ profiles over 12 h.
- the vertical structure of the energy-flux profile is qualitatively captured by as few as $n = 4$ profiles.
- if spectral peaks are distinct, harmonic analyses applied to regularly-sampled time-series are effective at rejecting contamination from other narrowband frequencies, but only slightly reduce the error associated with broadband GM contamination.
- wave advection of strong meso- and submesoscale fronts only weakly contaminates the depth integrated energy flux (Appendix A).
- harmonic analyses should not be used to analyze sparsely-sampled time-series with non-uniform sample spacing, because GM and near-inertial contamination can alias unpredictably into the wave of interest.

We also considered the case of temporally well-sampled but vertically gappy data, as in the case of discretely-instrumented moorings or partial-water-column moored profilers. Here, temporal contamination can be eliminated via filtering or harmonic analysis, but normal-mode fits must be employed via least-squares

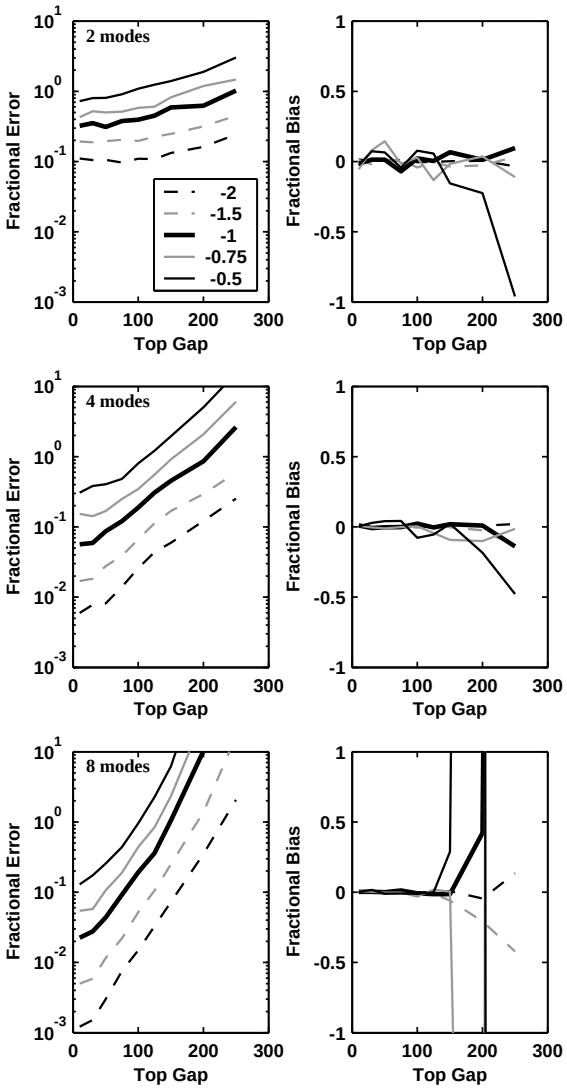

FIG. 8. Fractional error (left) and bias (right) computed from Monte-Carlo simulations for well-resolved profiles with varying gaps near the surface. Each curve represents the error/bias versus gap length for a particular slope of the ocean spectrum. Top, middle and bottom panels represent 2-, 4- and 8-mode solutions, respectively. Higher-mode solutions are more precise, but become unstable for smaller gaps.

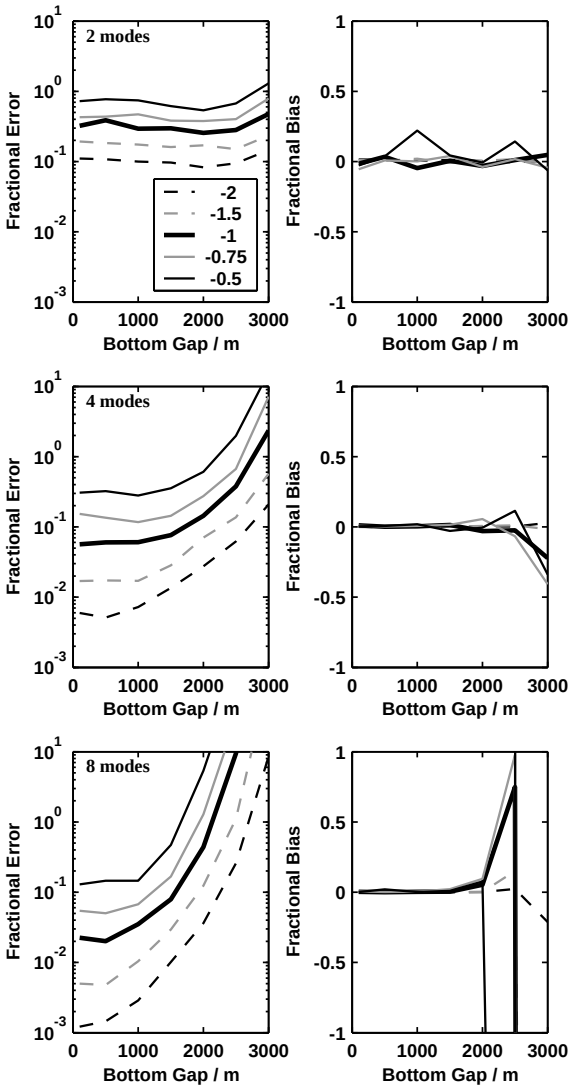

FIG. 9. As in Figure 8 but for gaps at the bottom.

methods to determine the necessary depth-integrals. We find the error to be highly sensitive to the slope of the internal-tide spectrum. Bluer ocean spectra and sparser measurements yield poorer fits and larger fractional errors in the energy flux.

Our specific results for the vertically-deficient case include

- For a "typical" mooring with 6 ideally-placed instruments and the HOME spectrum, the fractional error is 40%.
- Estimates are unbiased, except in the case of very large gaps at top or bottom.
- Estimates are sensitive to data near the surface. Errors increase rapidly as the depth of the top measurement increases.
- Due to the WKB weighting of energy flux, larger gaps can be tolerated at the bottom than at the top.
- In all cases, solving for more modes reduces the error, but can affect the stability of the solutions if modes with a wavelength comparable to the WKB-stretched gap are solved for.

We conclude with a final cautionary note that even perfectly-resolved flux estimates have subtleties that can

require care in their interpretation. For example, Nash et al. (2004a,b) considered a horizontal standing pattern resulting from two internal tides propagating in opposite directions. In such cases, the flux in the transverse direction displays a spatial periodicity, requiring spatial as well as temporal averaging. Naive consideration of its unaveraged divergence would lead to spurious conclusions.

Appendix A: Wave advection of horizontal gradients

Horizontal density and velocity gradients associated with meso- and submesoscale variability are advected by wave motions and contribute to u' and p' as measured at fixed (x_o, y_o). This appendix assesses the importance of u'_{adv} and p'_{adv} in contaminating $\mathbf{F_E}$ estimates [i.e, through eq. (10)].

Consider a wavefield with velocity $\mathbf{u'_{wave}} \equiv \mathbf{u'_{M_2}} + \mathbf{u'_f} + \mathbf{u'_{GM}}$. At time t', the fluid at position $\mathbf{x_o}$ was located at $\mathbf{x_{adv}} = \mathbf{x_o} - \int_{t_o}^{t'} \mathbf{u'_{wave}}\, dt$ at time $t = t_o$. The advective contribution to ρ at t' is therefore $\rho_{adv} = \rho_o(\mathbf{x_{adv}}) - \rho_o(\mathbf{x_o})$ and will produce a pressure perturbation p_{adv} through the hydrostatic balance. Similarly, the advective contributions to u' and v' at t' are $u_{adv} = u_o(\mathbf{x_{adv}}) - u_o(\mathbf{x_o})$ and $v_{adv} = v_o(\mathbf{x_{adv}}) - v_o(\mathbf{x_o})$.

For the purpose of this analysis, we assume that u_o, v_o and ρ_o correspond to a surface-intensified front in geostrophic balance with level-of-no-motion at $z = -500$ m. Our benchmark case ($a_{front} = 1$) corresponds to a series of 10-km wide fronts with 20-m peak-to-peak vertical displacements that induce $\pm$0.9 m/s surface currents and a $\pm$0.43 m/s maximum average velocity in the upper 500 m. Frontal vertical displacements vary periodically in x as $\xi_o = a_{front}\xi_{max}\cos(2\pi x/\lambda)Z(z)$, where $\xi_{max} = 10$ m, $\lambda = 20$ km, and $Z(z)$ is piecewise linear in the vertical (increasing from 0 to 1 between 0 and -200 m, returning to 0 at -500 m. For $a_{front} = 1$, the mean surface velocity gradient $\langle|du_o/dy|\rangle$ is 0.18 m/s per km. These gradients are extremely sharp and their vertical structure projects strongly into mode-1. Hence, we consider this to represent a worst-case scenario for advective contamination.

A front varying only with x is advected by the $\hat{i}$-component of wave velocity u'_{wave}. This produces no u_{adv} since $u_o = 0$ in the front (only $v_o \neq 0$). Conversely, a front varying only with y is advected by v'_{wave} and alters u' through u_{adv}; because $v_{adv} = 0$, v' is unaltered. It is thus necessary to consider both velocity components of the wavefield in addition to their orientation with respect to the front.

We employ the Monte Carlo techniques of section 4 to assess the cumulative effect of all terms in (10) involving u'_{adv} and p'_{adv} (as well as those in the $v'p'$ equation involving v_{adv}). Simulations were performed in which fronts were oriented in either $\hat{i}$ and $\hat{j}$ directions. For each frontal orientation, two sensitivity studies were conducted: (1) frontal amplitudes were varied from $0 < a_{front} < 2$ while holding $a_{wave} = 1$ fixed; (2) semidiurnal wave amplitudes were varied from $0 < a_{wave} < 2$ while holding $a_{front} = 1$ fixed. a_{wave} represents the total wave amplitude so that $a_{M2} = a_f = a_{GM} = a_{wave}$ were co-varied together. For each case, the error and bias was computed from 200 independent realizations with randomly phased wavefields superimposed onto randomly located fronts. In all cases, we assume perfect temporal and spatial sampling and compute estimates using harmonic analysis. The results of these simulations are summarized in Fig. A1.

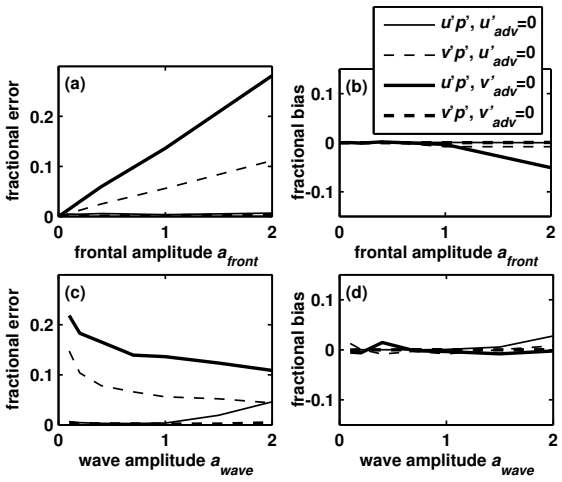

FIG. A1. Sensitivity of fractional error and bias of the depth-integrated energy flux to contamination from horizontal advection of a 10-km wide geostrophic front, as computed from Monte Carlo simulations (see Fig. 4). (a,b) represent fractional error and bias as a function of frontal strength a_{front}; (c,d) represent fractional error and bias as a function of internal wave strength a_{wave}. Thin lines represent simulations in which the front is oriented with gradients in the $\hat{i}$ direction so that $(v'_{adv},\ p'_{adv}) = f(v_o(x), \rho_o(x)),\ u'_{adv} = 0$; thick lines represent a front oriented with gradients in the $\hat{j}$ direction so that $(u'_{adv},\ p'_{adv}) = f(u_o(y), \rho_o(y)),\ v'_{adv} = 0$. Solid lines represent statistics of the major-axis energy flux $u'p'$; dashed lines the minor-axis $v'p'$. All data are normalized by the major-axis energy flux $|\int F_E^{M_2} dz|$, as in Fig. 4; error is represented as a standard deviation.

Despite the strength of the prescribed front, the advective contamination into F_E is weak compared to the sampling error presented in section 4. Estimates are unbiased and contamination is restricted to the component of energy flux parallel to the frontal velocity. That is, a front with $u_o = 0$ does not alter the $\hat{i}$-component of the energy flux. This is because the advection of ρ_o does not contaminate F_E since both ρ_{adv} and the induced p'_{adv} are in quadrature with u'_{M2}. Hence only the advection of frontal velocities alters the energy flux so that the error increases linearly with a_{front}. For fixed a_{front}, absolute error increases roughly with the square of wave strength, because both velocity contamination u'_{adv} and the pressure perturbation p'_{wave} scale linearly with a_{wave}, and the induced

error is dominated by the correlation $\langle u'_{adv} p'_{wave} \rangle$. The fractional error, however, decreases slightly with wave strength because both F_E and the advected contamination scale approximately with a^2_{wave}.

In contrast to the depth-integrated estimates, the energy flux at a given depth within the upper 500-m has a standard error $\sigma \sim 10\,\mathrm{W\,m^{-2}}$, comparable to that associated with sampling errors (Fig. 3). Hence, advection can strongly contaminate the flux profile while only weakly altering its depth integral. This is the direct result of the weak role of p'_{adv} in advective contamination, and the much higher-wavenumber content of u'.

In summary, the advection of a surface intensified front with 1.8 m/s change in u over 10 km contaminates the depth integrated energy flux by less than 20%. We conclude that frontal advection is not likely to strongly contaminate $\int F_E dz$. While the profile $F_E(z)$ may be contaminated by this extremely strong front, more typical frontal strengths will induce errors much smaller error in $F_E(z)$ than that associated with discrete sampling.

Appendix B: Generating GM depth/time series

We wished to "contaminate" the tidal signals in the Monte-Carlo simulations with time-depth series of velocity and displacement, $u_{GM}(z,t), \xi_{GM}(z,t)$ that have the Garrett-Munk spectrum, $\Phi^u_{GM}(k_z,\omega), \Phi^\xi_{GM}(k_z,\omega)$. Since the GM spectrum is separable by assumption, $\Phi_{GM}(k_z,\omega) = \Phi^\omega_{GM}(\omega)\ \Phi^{k_z}_{GM}(k_z)$ for both u and ξ. Essentially, we create Fourier amplitudes with this spectrum, randomize their phases, and inverse transform. Here we outline the detailed procedure for generating $u_{GM}(z,t)$; the procedure for $\xi_{GM}(z,t)$ is the same.

For each realization, we generated a matrix of amplitudes, $\tilde{u}_{GM}(k_z,\omega)$ that was consistent with GM75 wavenumber and frequency spectra (Cairns and Williams 1976); i.e. $\tilde{u}\tilde{u}^* = \Phi^u_{GM}(k_z,\omega)$. This was done for a set of discrete frequencies and wavenumbers, $0 < \omega < \omega_N, 0 < k_z < k_{zN}$, where the subscript N indicates the Nyquist frequency or wavenumber. We then randomized the phase of each amplitude by multiplying each by $e^{i\Psi}$, where $0 \le \Psi \le 2\,\pi$ is a uniformly distributed random variable.

The amplitudes were then mirrored across zero frequency such that $\tilde{u}(-\omega) = \tilde{u}^*(\omega)$, to ensure real series. (There is no enforced phase relation between k_z and -k_z, allowing both vertically standing and propagating contributions.) At this point, the dimension of the amplitude matrix was the same as that of the desired time/depth series.

The amplitudes were then inverse 2-D Fourier transformed, producing a depth-time series $u^{WKB}(z',t)$ with the correct spectrum. However, the wavelength and amplitude are stationary in depth. That is, they mimic "true" ocean field after WKB stretching and scaling to remove refractive effects. The final "ocean" contaminant depth-time series were produced by WKB "un-stretching" using (5a), and "un-scaling" using $u_{GM}(z) = u^{WKB}_{GM}\,(\frac{N(z)}{N_o})^{\frac{1}{2}}$.

Acknowledgements. The authors thank Tom Sanford, Craig Lee and the technical support of the Applied Physics Lab (John Dunlap, Art Bartlett, and Bob Drever) for making these measurements possible. J.N. and E.K. were supported by NSF grant OCE-98-19537 and ONR grant N00014-97-10087. M.A.'s contribution to this work was supported by the Office of Naval Research Young Investigator award, grant N00014-02-10526.

REFERENCES

Alford, M. and M. Gregg, 2001: Near-inertial mixing: Modulation of shear, strain and microstructure at low latitude. *J. Geophys. Res.*, **106**, 16947–16968.

Alford, M. H., 2003: Energy available for ocean mixing redistributed by long-range propagation of internal waves. *Nature*, **423**, 159–162.

Althaus, A. M., E. Kunze, and T. B. Sanford, 2003: Internal tide radiation from Mendicino Escarpment. *J. Phys. Oceanogr.*, **33**, 1510–1527.

Baines, P. G., 1982: On internal tide generation models. *Deep Sea Res.*, **29**, 307–338.

Baumert, H. and H. Peters, 2004: Turbulence closure, steady state and collapse into waves. *Journal of Physical Oceanography*, **34**, 505–512.

Bell, T. H., 1975: Topographically generated internal waves in the open ocean. *J. Geophys. Res.*, **80**, 320–327.

Cairns, J. L. and G. O. Williams, 1976: Internal wave observations from a midwater float, 2. *J. Geophys. Res.*, **81**, 1943–1950.

Carter, G. S. and M. C. Gregg, 2002: Intense variable mixing near the head of Monterey Submarine Canyon. *J. Phys. Oceanogr.*, **32**, 3145–3165.

Cummins, P. F., J. Y. Cherniawski, and M. G. Foreman, 2001: North Pacific internal tides from the Aleutian Ridge: Altimeter observations and modelling. *J. Mar. Res.*, **59**, 167–191.

Cummins, P. F. and L. Y. Oey, 1997: Simulation of barotropic and baroclinic off northern Britich Columbia. *J. Phys. Oceanogr.*, **27**, 762–780.

D'Asaro, E., C. E. Eriksen, M. D. Levine, P. Niiler, C. A. Paulson, and P. V. Meurs, 1995: Upper-ocean inertial currents forced by a strong storm, I, Data and comparisons with linear theory. *J. Phys. Oceanogr.*, **25**, 2909–2936.

Dushaw, B., B. Cuornelle, P. F. Worcester, B. Howe, and D. Luther, 1995: Barotropic and baroclinic tides in the Central North Pacific Ocean determined from long-range reciprocal acoustic transmissions. *Journal of Physical Oceanography*, **25**, 631–647.

Emery, W. J. and R. E. Thomson, 2001: *Data Analysis Methods in Physical Oceanography*. Elsevier Science B.V., Amsterdam, The Netherlands, 2nd edition.

Garcia Lafuente, J., T. Sarhan, M. Vargas, J. Vargas, and F. Plaza, 1999: Tidal motions and tidally-induced fluxes through La Linea submarine canyon, western Alboran Sea. *J. Geophys. Res.*, 3109–3119.

Johnson, G. C., R. G. Lueck, and T. B. Sanford, 1994a: Stress on the Mediterranean outflow plume: Part II. turbulent dissipation and shear measurements. *J. Phys. Oceanogr.*, **24**, 2084–2092.

Johnson, G. C., T. B. Sanford, and M. O. Baringer, 1994b: Stress on the Mediterranean outflow plume; part I, Velocity and water property measurements. *J. Phys. Oceanogr.*, **24**, 2072–2083.

Kunze, E., L. K. Rosenfeld, G. S. Carter, and M. C. Gregg, 2002: Internal waves in Monterey Submarine Canyon. *J. Phys. Oceanogr.*, **32**, 1890–1913.

Kunze, E. and T. B. Sanford, 1984: Observations of near-inertial waves in a front. *J. Phys. Oceanogr.*, **14**, 566–581.

Kunze, E., R. W. Schmitt, and J. M. Toole, 1995: The energy balance in a warm-core ring's near-inertial critical layer. *J. Phys. Oceanogr.*, **25**, 942–957.

Large, W., J. McWilliams, and S. Doney, 1994: Oceanic vertical mixing: A review and a model with a nonlocal boundary-layer parameterization. *Rev. Geophys. Space Phys.*, **32**, 363–403.

Lee, C. M., E. Kunze, T. B. Sanford, , J. D. Nash, M. A. Merrifield, and P. E. Holloway, 2005: Internal tides and turbulence along the 3000-m isobath of the Hawaiian Ridge. *J. Phys. Oceanogr.*, submitted.

Levine, M. D. and T. J. Boyd, 2004: Tidally-forced internal waves and overturns observed on a slope: Results from the HOME survey component. *J. Phys. Oceanogr.*, submitted.

MacKinnon, J. A. and M. C. Gregg, 2003: Shear and baroclinic energy flux on the summer New England Shelf. *Journal of Physical Oceanography*, **33**, 1462–1475.

Mellor, G. L. and T. Yamada, 1982: A hierachy of turbulence closure models for planetary boundary layers. *J. Atmos. Sci.*, **31**, 1791–1806.

Merrifield, M. A. and P. E. Holloway, 2002: Model estimates of m_2 internal tide energetics at the Hawaiian Ridge. *J. Geophys. Res.*, **107**, doi:10.1029/2001JC000996.

Merrifield, M. A., P. E. Holloway, and T. M. S. Johnston, 2001: Internal tide generation at the Hawaiian Ridge. *Geophys. Res. Let.*, **28**, 559–562.

Mied, R., C. Shen, C. Trump, and G. Lindemann, 1986: Internal-inertial waves in a Sargasso Sea front. *Journal of Physical Oceanography*, **16**, 1751–1762.

Munk, W. and C. Wunsch, 1998: Abyssal recipes II: energetics of tidal and wind mixing. *Deep Sea Res.*, **45**, 1977–2010.

Nash, J. D., E. Kunze, C. M. Lee, and T. B. Sanford, 2004a: Structure of the baroclinic tide generated at Kaena Ridge, Hawaii. *J. Phys. Oceanogr.*, **xx**, xxx–xxx.

Nash, J. D., E. Kunze, J. M. Toole, and R. W. Schmitt, 2004b: Internal tide reflection and turbulent mixing on the continental slope. *J. Phys. Oceanogr.*, **34**, 1117–1134.

Price, J. F., R. A. Weller, and R. Pinkel, 1986: Diurnal cycling: Observations and models of the upper ocean response to diurnal heating, cooling, and wind mixing. *J. Geophys. Res.*, **91**, 8411–8427.

Rainville, L. and R. Pinkel, 2005: Baroclinic energy flux at the Hawaiian Ridge: Observations from the R/P FLIP. Submitted.

Ray, R. D. and G. T. Mitchum, 1997: Surface manifestation of internal tides in the deep ocean: Observations from altimetry and island gauges. *Prog. Oceanogr.*, **40**, 135–162.

Rudnick, D. L., T. J. Boyd, R. E. Brainard, G. S. Carter, G. D. Egbert, M. C. Gregg, P. E. Holloway, J. M. Klymak, E. Kunze, C. M. Lee, M. D. Levine, D. S. Luther, J. P. Martin, M. A. Merrifield, J. N. Moum, J. D. Nash, R. Pinkel, L. Rainville, and T. B. Sanford, 2003: From tides to mixing along the Hawaiian Ridge. *Science*, **301**, 355–357.

Sanford, T. B., R. G. Drever, and J. H. Dunlap, 1978: A velocity profiler based on the principles of geomagnetic induction. *Deep Sea Res.*, **25**, 183–210.

— 1985: An acoustic Doppler and electromagnetic velocity profiler. *J. Atmos. Oceanic Technol.*, **2**, 110–124.

Simmons, H. L., R. W. Hallberg, and B. K. Arbic, 2004: Internal wave generation in a global baroclinic tide model. *Deep-Sea Res II*, 1–20, submitted.

Wunsch, C., 1975: Internal tides in the ocean. *Rev. Geophys.*, **13**, 167–182.

---

submitted

Generated with ametsocjtech.cls.

Thanks to J. M. Klymak